ADVANCED MATERIALS

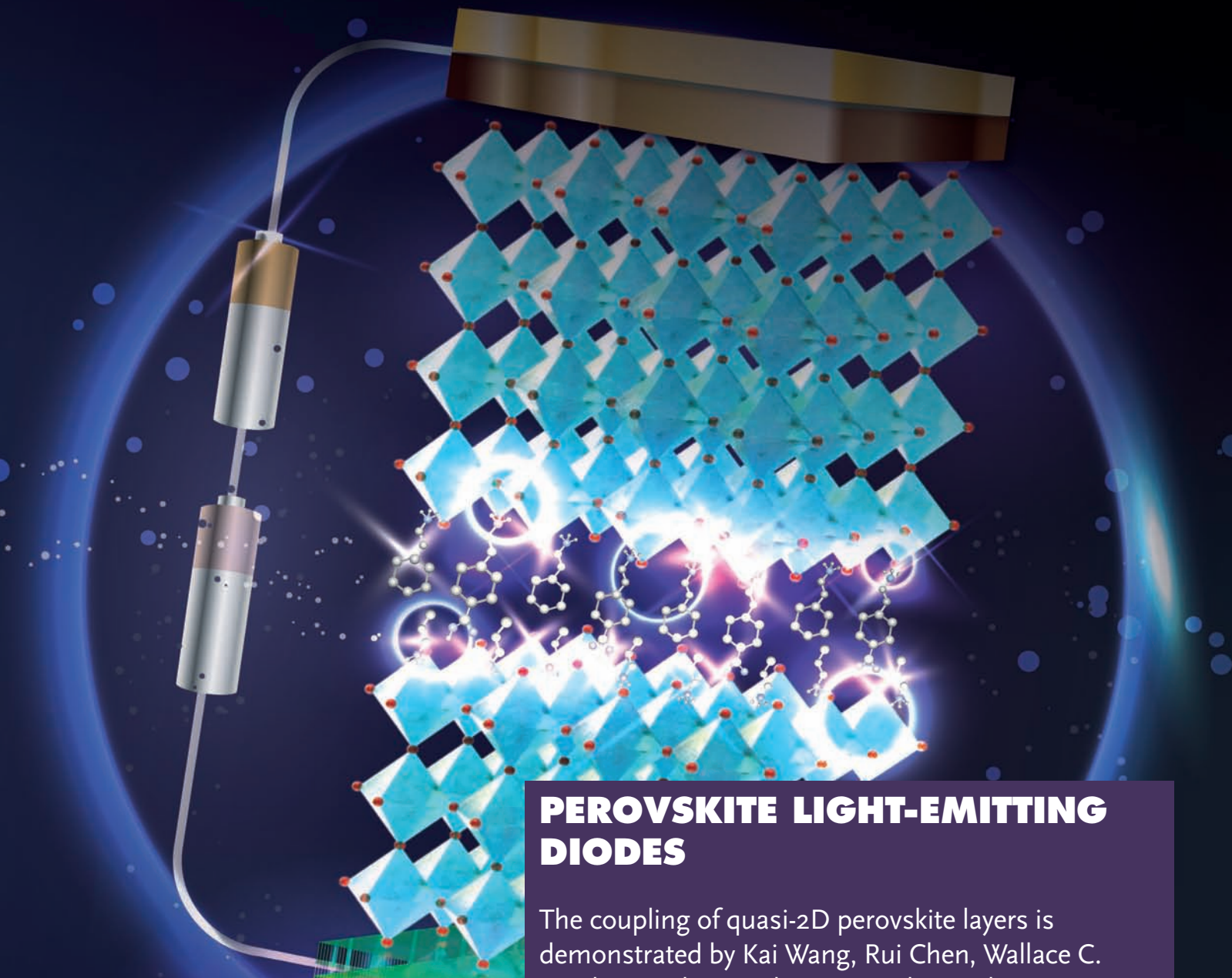

PEROVSKITE LIGHT-EMITTING DIODES

The coupling of quasi-2D perovskite layers is demonstrated by Kai Wang, Rui Chen, Wallace C. H. Choy, and co-workers in article number 2005570. Their results show that a bifunctional ligand can simultaneously diminish the weak van der Waals gap and passivate perovskite defects for efficient energy transfer and radiative recombination. They fabricate blue PeLEDs that show high performance with an EQE of 10.11% and a long stability of 81.3 min.

WILEY-VCH

ADVANCED MATERIALS
www.advmat.de

High-Performance Blue Perovskite Light-Emitting Diodes Enabled by Efficient Energy Transfer between Coupled Quasi-2D Perovskite Layers

Zhenwei Ren, Jiahao Yu, Zhaotong Qin, Jing Wang, Jiayun Sun, Christopher C. S. Chan, Shihao Ding, Kai Wang, Rui Chen,* Kam Sing Wong, Xinhui Lu, Wan-Jian Yin, and Wallace C. H. Choy**

While there has been extensive investigation into modulating quasi-2D perovskite compositions in light-emitting diodes (LEDs) for promoting their electroluminescence, very few reports have studied approaches involving enhancement of the energy transfer between quasi-2D perovskite layers of the film, which plays very important role for achieving high-performance perovskite LEDs (PeLEDs). In this work, a bifunctional ligand of 4-(2-aminoethyl)benzoic acid (ABA) cation is strategically introduced into the perovskite to diminish the weak van der Waals gap between individual perovskite layers for promoting coupled quasi-2D perovskite layers. In particular, the strengthened interaction between coupled quasi-2D perovskite layers favors an efficient energy transfer in the perovskite films. The introduced ABA can also simultaneously passivate the perovskite defects by reducing metallic Pb for less nonradiative recombination loss. Benefiting from the advanced properties of ABA incorporated perovskites, highly efficient blue PeLEDs with external quantum efficiency of 10.11% and a very long operational stability of 81.3 min, among the best performing blue quasi-2D PeLEDs, are achieved. Consequently, this work contributes an effective approach for high-performance and stable blue PeLEDs toward practical applications.

Metal halide perovskites have emerged as competitive candidates for the next-generation light-emitting diodes (LEDs) due to their excellent optical properties, such as tunable light emission color, high color purity, and high photoluminescence quantum yields (PLQYs).[1–7] Recently, impressive external quantum efficiencies (EQEs) exceeding 20% are obtained for green, red, and near-infrared perovskite-based LEDs (PeLEDs) through the efforts of perovskite material optimization and device architecture design.[8–10] These achievements firmly prompt the potential applications of PeLEDs in display and illumination fields. However, compared with the efficient PeLEDs, there is only moderate performance reported for blue PeLEDs,[11–18] which undoubtedly restrict PeLED applications in full-color displays and white-light illumination. Thus, the breakthroughs of the device performance are urgently required for blue PeLEDs.

Substantial efforts have been made in the past several years to obtain blue perovskite emitters, such as perovskite nanocrystals (NCs),[19–25] 2D perovskite nanoplatelets,[26–32] and quasi-2D perovskites.[33–39] In particular, the quasi-2D perovskites are rising as efficient luminescent materials for highly performed blue PeLEDs due to the cascade energy landscape for efficient exciton transfer and the subsequent radiative recombination. Typically, the quasi-2D perovskites have a formula of $B_2(APbBr_3)_{n-1}PbBr_4$,

Z. Ren, J. Sun, Prof. W. C. H. Choy
Department of Electrical and Electronic Engineering
The University of Hong Kong
Pokfulam Road, Hong Kong, China
E-mail: chchoy@eee.hku.hk

J. Yu, S. Ding, Prof. K. Wang, Prof. R. Chen
Department of Electrical and Electronic Engineering
Southern University of Science and Technology
Shenzhen 518055, China
E-mail: wangk@sustc.edu.cn; chenr@sustech.edu.cn

Z. Qin, Prof. X. Lu
Department of Physics
The Chinese University of Hong Kong
Shatin, Hong Kong, China

J. Wang, Prof. W.-J. Yin
College of Energy
Soochow Institute for Energy and Materials InnovationS (SIEMIS)
Soochow University
Suzhou 215006, China

C. C. S. Chan, Prof. K. S. Wong
Department of Physics
Hong Kong University of Science and Technology
Clear Water Bay, Hong Kong, China

Prof. W. C. H. Choy
Guangdong-Hong Kong-Macao Joint Laboratory for
Photonic-Thermal-Electrical Energy Materials and Devices
Shenzhen 518055, China

The ORCID identification number(s) for the author(s) of this article can be found under https://doi.org/10.1002/adma.202005570.

DOI: 10.1002/adma.202005570

where B is an organic spacer cation, A is a monovalent cation (e.g., Cs , methylammonium (MA) or formamidinium, (FA)), and *n* represents the number of lead halide octahedral layers.[40,41] The organic spacer cations play a vital role in modulation of perovskite properties, such as the emission peak, structural morphology, defect level, phase distribution, and thus the PeLED performances. For example, Yip et al. reported a structural modulated quasi-2D perovskite through adopting the spacer cation of 2-phenoxyethylamine, and obtained an EQE of 1.1% for the blue PeLEDs.[17] They further introduced phenylethylammonium bromide (PEABr) into the $CsPbCl_{0.9}Br_{2.1}$ to form a quasi-2D perovskite with effective suppression of traps, and achieved 5.7% efficiency at 480 nm.[42] Jin et al. reported utilization of phenylbutylamine bromide (PBABr) as the spacer cation to construct $PBABr_y(Cs_{0.7}FA_{0.3}PbBr_3)$ with perovskite nanoparticles (NPs) embedded in quasi-2D phases, and obtained an EQE of 9.5% and lifetime of 250 s for the blue PeLEDs.[43] In addition, the joint organic cations, such as PEABr and butylammonium bromide (BABr),[34] PEABr and propylammonium bromide (PABr),[44] PEABr and iso-propylammonium bromide (IPABr),[39,45] and 1,4-Bis(aminomethyl) benzene bromide (P-PDABr_2) and PEABr[46] were also employed as the spacer cations to modulate the quasi-2D perovskite phase distribution for high phase purity and thus efficient light emission. Besides optimizing the organic spacer cations in quasi-2D perovskites, the composition of "A-site" has been also tuned to prolong PeLED operational stability, such as rubidium-cesium alloyed quasi-2D $PEA_2(Rb_xCs_{1-x})_{n-1}PbnBr_{3n\ 1}$ perovskite,[47] and mixture of monovalent cation perovskite (e.g., $PEA_2(Cs/Rb/FA/K)Pb_n\ (Cl/Br)_{3n\ 1}$[48]). Recently, another strategy of incorporating yttrium chloride into the quasi-2D perovskite was reported, in which the charge carriers were confined inside perovskite grains for efficient radiative recombination, and the blue PeLED efficiency of 11% was achieved.[49]

It is known that quasi-2D perovskites usually contain a mixture of phases and the phase impurity (especially a wide distribution and large amount of low-order phases) could result in low emission efficiency due to inefficient internal energy transfer.[40,47] Thus fine control of the quasi-2D perovskite composition for high phase purity is a good approach to promote internal energy transfer for improved PeLED efficiency.[34,39,46,50] Besides, it is noted that the quasi-2D perovskite layers are separated from each other by spacer cations. Typical spacer cations, such as PEA , BA can only interact with the perovskite layers at one side and leave a van der Waals gap with other quasi-2D perovskite layers.[51,52] It is thus a concern that the van der Waals gap will induce a loose space between quasi-2D perovskite layers and subsequently inefficient energy transfer in the perovskite film causing poor PeLED efficiency. Besides, the presence of weak van der Waals gaps also deteriorates the stability of quasi-2D perovskite structure due to easy degradation of perovskite structure upon exposure to different operation conditions, such as continuous heat and light soaking during PeLED operation.[52] Consequently, reduction of the van der Waals gaps and strengthened interaction between quasi-2D perovskite layers are very important to obtain well-performed PeLEDs.

In this work, we introduce a bifunctional ligand of 4-(2-Aminoethyl)benzoic acid (ABA) cation into the perovskite to diminish the weak van der Waals gaps for promoting the coupling of quasi-2D perovskite layers via the bifunctional group of amino and carboxylic. The strengthened interaction between coupled quasi-2D perovskite layers benefits an efficient energy transfer intrinsically in the ABA incorporated perovskite films for highly performed PeLEDs. Besides, we show that the ABA can reduce traps states and thus nonradiative recombination loss by suppressing the metallic Pb in the perovskite film. By optimizing the new type of quasi-2D perovskite, the blue PeLEDs achieve high external quantum efficiency of 10.11% and a prolonged operational stability of 81.3 min. Consequently, this work contributes to evolving approaches for the realization of highly performed and stable blue PeLEDs.

The coupled quasi-2D perovskites were constructed based on the mixed-ligand perovskite of $PEA_xPA_{2-x}(CsPbBr_3)_{n-1}PbBr_4$ (0 x 2) which is hereafter named as pristine perovskite. In the pristine perovskite, the perovskite phases were redistributed with an increasement of high-order phases (e.g., n 3 phase) via suppression of low-order phases (e.g., n 2 phase) (Figure S1, Supporting Information). However, inevitable van der Waals gaps are formed in the pristine perovskites due to the spacer organic monoammonium cations, such as PEA and PA , which result in weak interactions between the quasi-2D perovskite layers (**Figure 1**a) and poor spectral stability (Figure S2, Supporting Information). When the ABA is incorporated into the pristine perovskite (denoted as pristine/ABA perovskite), the weak van der Waals gaps can be diminished, and the interaction between perovskite layers is strengthened through the bifunctional group of amino and carboxylic of ABA (Figure 1b). The close interaction of the coupled quasi-2D perovskite layers will promote an efficient energy transfer between the perovskite layers and thus enhance the radiative recombination rate of the perovskite films as to be discussed later.

The molecular structure of ABA is shown in Figure 1b, which consists of amino, carboxylic acid, and phenethyl groups. To analyze the interaction between ABA and the perovskite layer (mainly the Pb-Br framework), Fourier transform infrared spectroscopy (FT-IR) was performed on ABA and ABA incorporated $PbBr_2$ powder (denoted as ABA/$PbBr_2$) to rule out the unexpected inf uence of other ammonium cations in the perovskite precursor. As shown in Figure 1c, the characteristic C=O stretching vibration peak is located at 1696 cm^{-1} for ABA, which shifts to a lower wavenumber of 1688 cm^{-1} for ABA/$PbBr_2$ powder, attributed to the strong interaction between −COOH and $PbBr_2$ through sharing the lone pair electron on the oxygen atom of −COOH with the empty 6p orbital of Pb^2 .[53,54] Meanwhile, the characteristic peaks observed at 1583 and 3483 cm^{-1} for ABA can be ascribed to the scissoring and stretching vibration of N−H, which shift to lower wavenumbers of 1576 and 3465 cm^{-1} for ABA/$PbBr_2$, respectively, due to the interaction between the N−H and the Pb-Br framework through hydrogen bond.[46,55] To further confirm the interaction between the ABA and the Pb-Br framework, X-ray photoelectron spectroscopy (XPS) measurements were performed. The peaks at143.3 and 138.4 eV for the pristine perovskite are assigned to Pb 4f signal, which shift toward lower binding energy upon incorporation of ABA (Figure 1d). The reduced binding energy indicates the lowered oxidation state of lead due to the electron donation from oxygen, which well agrees with the FT-IR results. In addition,

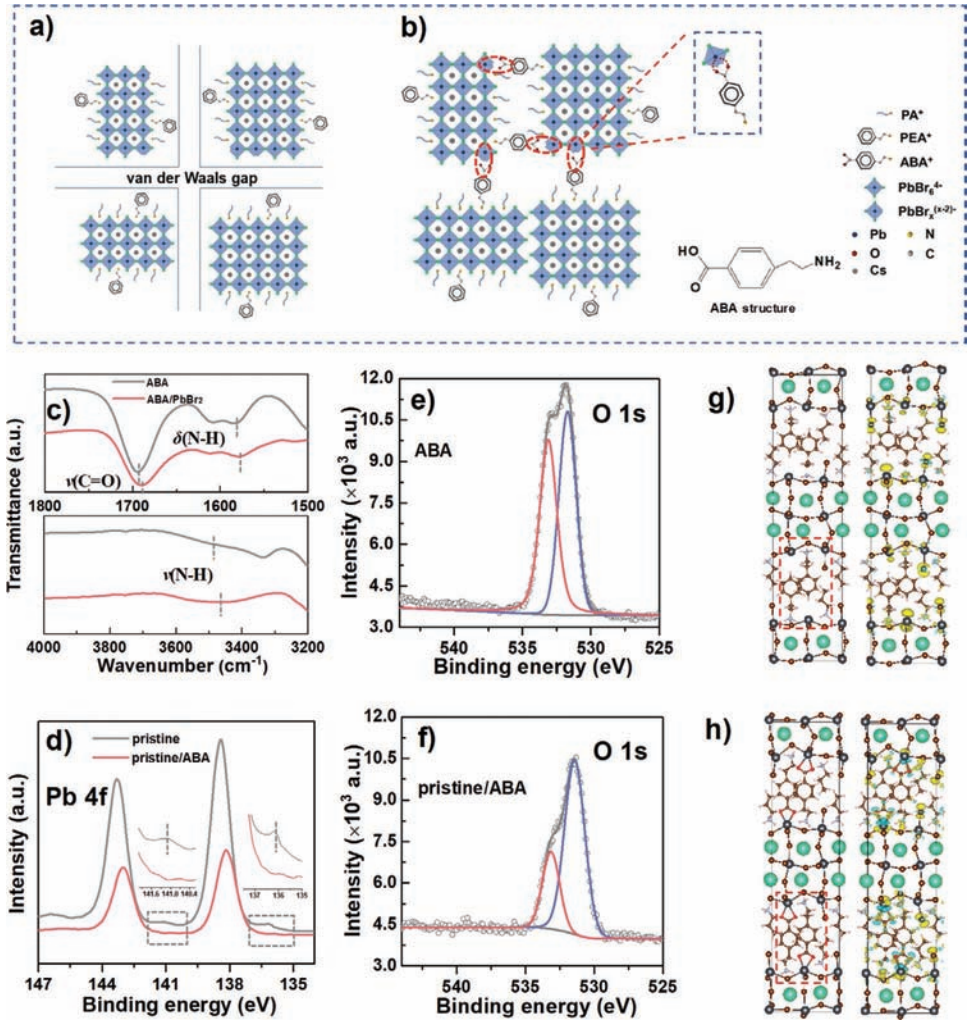

Figure 1. Schematic illustration of a) pristine, b) pristine/ABA perovskite, and the interaction between neighboring perovskite layers in pristine/ABA perovskite. c) FT-IR spectroscopy of ABA and ABA incorporated $PbBr_2$ powder. XPS spectra: d) Pb 4f signal of pristine and pristine/ABA perovskites (inset: enlarged views extracted from the dashed boxes), and e,f) O 1s signals of ABA and its incorporated perovskite films. DFT calculations of g) pristine and h) ABA incorporated perovskites, and their deformation charge density distributions.

the signals of metallic Pb were observed in the pristine perovskite film, as evidenced by the two weak peaks located at 141.1 and 136.2 eV.[56] In contrast, no metallic Pb peak is found in pristine/ABA perovskite film, which indicates that the formation of metallic Pb is suppressed. Since the presence of metallic Pb species was reported to closely relate with halide vacancies in the perovskite lattice,[56,57] the suppression of metallic Pb for ABA incorporated perovskite film suggests that the bromide vacancies are effectively passivated by ABA. Moreover, the O 1s signals of ABA and the incorporated perovskite films were recorded to further verify the interaction of oxygen atom and Pb^2 (Figure 1e,f). As shown in the spectra, the observed broad peaks can be deconvoluted into two peaks at 531.4 and 533.1 eV, which are assigned to oxygen from the components of C=O and C−O in carboxylic acid group, respectively.[58] It is found that the peak intensity of C=O and C−O declines after ABA incorporation in the perovskite due to the weakened C=O and C−O bonds, which indicates both of the oxygen atoms from C=O and C−O have strong interactions with Pb^2 . Besides, the density functional theory (DFT) calculations were carried out to further theoretically reveal the interaction between ABA organic spacer and quasi-2D perovskites (Figure 1g,h). It is found that the ABA can coordinate the unsaturated Pb^2 through the coordination bond of Pb−O while only van der Waals interaction is observed between PEA cation spacer and octahedral layer in pristine perovskite. Specifically, the deformation charge density of pristine perovskites shows that the valence electrons are merely gathered and distributed near the separated atoms (e.g., hydrogen atom from PEA cation and lead atom from the octahedral layer) in pristine perovskite, indicating there is no bonding interaction between the PEA cation and perovskite layer. However, distinct charge transfer between oxygen and lead atoms is observed for ABA incorporated perovskite. Meanwhile, the distance between oxygen and lead atoms of 2.54 Å is comparable to the sum of their ionic radii of 2.59 Å (oxygen: 1.4 Å, lead: 1.19 Å). These results demonstrate a strong interaction between ABA and perovskite layer. Then the grazing-incidence wide-angle X-ray scattering measurements were carried

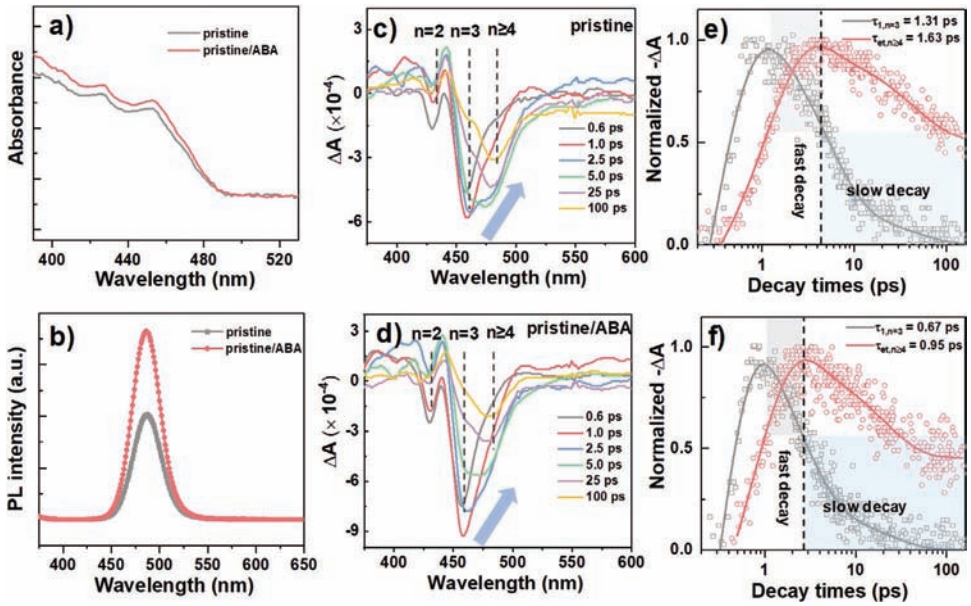

Figure 2. Optical properties of the perovskite films: a) The UV–visible absorption spectra and b) steady state photoluminescence of the pristine and pristine/ABA perovskite films. Transient absorption (TA) spectroscopy of the perovskite films: c,d) TA spectra at dif erent probe delay times, and e,f) TA kinetics probed at selected wavelengths (453 and 481 nm) for pristine and pristine/ABA perovskite films, respectively.

out to evaluate the effect of ABA on the perovskite phase orientation and distribution (Figure S3, Supporting Information). It is observed that the bright scatter halos are presented in both q_z and q_r directions for pristine and pristine/ABA perovskite films, indicating both parallelly and vertically oriented quasi-2D perovskites formed in the films.[59] The X-ray scattering profiles along the q_z direction of the films were plotted in Figure S4 (Supporting Information). It is found that the pristine/ABA perovskite film shows the same main characteristic peaks as compared to that of pristine perovskite film, indicating that the main perovskite phases remain unchanged by ABA incorporation. Meanwhile, an extra peak at 0.27 $Å^{-1}$ appears in pristine/ABA perovskites, which may be attributed to the interaction of quasi-2D perovskite layers (Figure S5b, Supporting Information). Overall, we demonstrate a strong interaction between ABA and perovskite layer through the functional groups of amino and carboxylic acid, which promotes the coupling of quasi-2D perovskite layers in the perovskite films. The strengthened interaction between the coupled perovskite phases will benefit the carrier transfer in the perovskite films as discussed later.

The UV–visible absorption spectra of the pristine and pristine/ABA perovskite films are shown in **Figure 2**a. The absorption spectra show two shoulders at around 428 and 453 nm for both pristine and pristine/ABA perovskite films, which are associated with the n 2 and n 3 layered perovskites, respectively, and a red-tail extending to 481 nm corresponding to n 4 perovskite phase.[39] However, their photoluminescence (PL) spectra only show a single PL peak centered at 486 nm (Figure 2b). Since the photogenerated carriers are driven from a larger bandgap (i.e., low-order) phase to a smaller bandgap (i.e., high-order) phase, and eventually recombine in high-order phase due to energy funneling effect, thus the single PL peak in the quasi-2D perovskite films suggests an energy transfer from the larger bandgap (i.e., n 2, n 3) phase to the smaller bandgap (i.e., n 4) phase (as illustrated in Figure S6, Supporting Information). To investigate the photogenerated carrier transfer dynamics in the pristine and pristine/ABA perovskites, the ultrafast transient absorption (TA) spectroscopy has been performed. The TA spectra of pristine and pristine/ABA perovskites at different timescales are shown in Figure 2c,d, in which three distinctive photobleaching (PB) peaks centered at 428, 453, and 481 nm are observed, corresponding to n 2, n 3, and n 4 phases in consistent with the absorption spectra. It can be observed that the photogenerated carriers are primarily formed in low order (i.e., n 2, n 3) phases with a fast buildup of n 2 and n 3 PB peaks at the initial stage (Figure 2c,d). When prolonging the decay time, the low-order PB peaks decrease accompanied with a gradual growth of the high-order (i.e., n 4) PB peak, indicating that the carriers transfer from low order phases to the high-order perovskites. To further study the carrier transfer process, time traces of low-order (e.g., n 3, 453 nm) phase and high-order (e.g., n 4, 481 nm) phase are extracted as shown in Figure 2e,f. The kinetics of each PB can be fitted by a multiexponential function: $A(t)$ $a_1 \exp(-t/\tau_1)$ $a_2 \exp(-t/\tau_2)$ $a_3 \exp(-t/\tau_3) - c_1 \exp(-t/\tau_{et})$, where a_1, a_2, a_3, and c_1 are amplitudes; τ_1 is the fast decay time constant due to the carrier transfer process in the perovskite; τ_2 and τ_3 represent the slow decay time constant; and τ_{et} is the formation time constant.[60] The fitting parameters were extracted and listed in Table S2 (Supporting Information). In pristine perovskite, the PB of n 3 phase shows a fast decay time with τ_1 of 1.31 ps (Figure 2e). The PB formation time of n 4 phase is 1.63 ps within the timescale of the fast decay time of n 3 phase, indicating a fast carrier transfer process. Differently, the PB of n 3 for pristine/ABA perovskites show a smaller τ_1 of 0.67 ps (Figure 2f), which is nearly half of that in pristine perovskite (1.31 ps), implying more efficient carrier

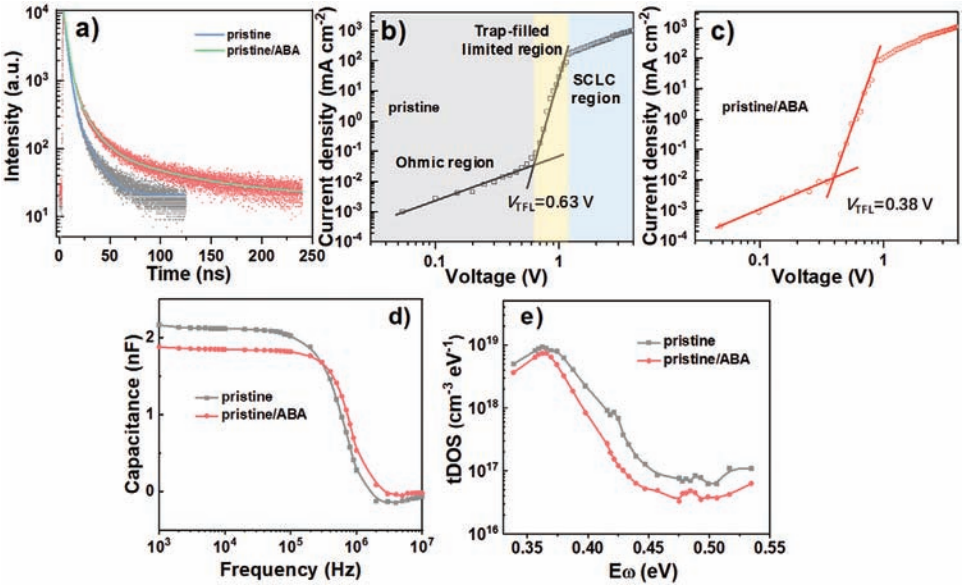

Figure 3. Characteristics of trap densities: a) The time-resolved photoluminescence (TRPL) decay spectra of the pristine and pristine/ABA perovskite films. The current–voltage (*J*–*V*) curves of b) pristine and c) pristine/ABA perovskite devices measured under dark condition with the structure of ITO/perovskite/MoO_3/Ag. d) The capacitance-frequency curves and e) trap density of states (*t*DOS) of pristine and pristine/ABA perovskites.

transfer from n 3 phase to n 4 phase in pristine/ABA perovskites. Besides, the higher efficient carrier transfer is verified by the faster formation time constant (τ_{et}, 0.95 ps) of n 4 phase for pristine/ABA perovskites, which is less than that of pristine perovskites (1.63 ps). Consequently, we observe the fast photogenerated carrier transfer from the low-order phase to the high-order phase in the quasi-2D perovskite, and demonstrate that pristine/ABA perovskites show more efficient carrier transfer from n 3 phase to n 4 phase than that of the pristine perovskite, which is vital to obtain highly performed PeLEDs as discussed in the following part.

Besides the efficient energy transfer in pristine/ABA perovskite films, there is an enhanced PL intensity for pristine/ABA perovskite films as observed in Figure 2b, consistent with this trend, a dramatic increase of PLQY from 45.5% (pristine) to 63.5% (pristine/ABA) is found (see Figure S7, Supporting Information), indicating a large reduction of nonradiative recombination. We further performed time-resolved PL (TRPL) measurements to investigate the effect of ABA on the perovskite film carrier lifetime. The TRPL decay curves are shown in **Figure 3**a, which can be fitted by a biexponential function of $I(t)$ I_0 $a_1 \exp(-t/\tau_1)$ $a_2 \exp(-t/\tau_2)$, where a_1, a_2 are the amplitudes; τ_1, τ_2 represent time constants for fast and slow decay lifetimes. The fast time constant is related to nonradiative recombination of the traps, and the slow time associates with the radiative recombination.[5,61] The fitted parameters for TRPL decay curves are extracted in Table S3 (Supporting Information). It is revealed that both the fast and slow decay lifetimes for pristine/ABA perovskite film of 3.62 and 19.63 ns are much longer than that of pristine perovskite film (τ_1, 3.08 ns and τ_2, 12.82 ns), which promotes the average f uorescence lifetime of pristine/ABA perovskite (τ_{av} 6.10 ns) 1.5-fold higher than the pristine perovskite (τ_{av} 3.99 ns). The PL and TRPL results show that the incorporation of ABA can effectively passivate trap states and improve the radiative recombination in the perovskite films, which is consistent with the result of the metallic Pb suppression by ABA incorporation as shown in Figure 1e. To further verify the effect of ABA on defect density of perovskite films, the space charge limited current (SCLC) is performed (Figure 3b,c). The current–voltage (*J*–*V*) curves of the devices were measured under dark condition with the structure of indium tin oxide (ITO)/perovskite/MoO_3/Ag. The trap state density of the perovskite film can be calculated by the equation of N $(2V_{TFL}\varepsilon_r\varepsilon_0)/(eL^2)$, where V_{TFL} is trap-filled limiting voltage, L is the thickness of the film, e represents the electron charge, ε_r and ε_0 are the dielectric constant and the vacuum permittivity, respectively. Generally, the lower value of V_{TEF} indicates the less concentration of trap states in the films. In order to determine the trap state density, the value of ε_r is estimated by the equation of ε_r $(CL)/(\varepsilon_0 S)$, where the geometrical capacitance of C can be determined from the *C*–*V* curves (Figure S8, Supporting Information), as reported previously.[42] As expected, the trap state density for pristine/ABA perovskite film is notably reduced to 2.01 10^{17} cm^{-3} from 4.22 10^{17} cm^{-3} (pristine perovskite film), which further confirms the effective passivation of ABA. Besides, we also extract the trap density of states (*t*DOS) of pristine and pristine/ABA perovskites from capacitance versus frequency measurement, in which the device structure of ITO/PVK/perovskite/TPBi/LiF/Al was adopted according to the previous reports.[55,62] As shown in Figure 3e, the pristine/ABA perovskite shows much lower *t*DOS that that of pristine perovskite over the entire energy range, indicating the less trap density after ABA incorporation, which is in good agreement with the results of TRPL and SCLC measurements.

We have also fabricated the PeLEDs to evaluate their EL performances. The PeLEDs are configured with a structure of ITO/PVK/perovskite/TPBi/LiF/Al, where the perovskite is the emission layer, PVK and TPBi are the hole injection layer (HIL) and electron injection layer (EIL), respectively. The energy bands of pristine and pristine/ABA perovskite films were confirmed

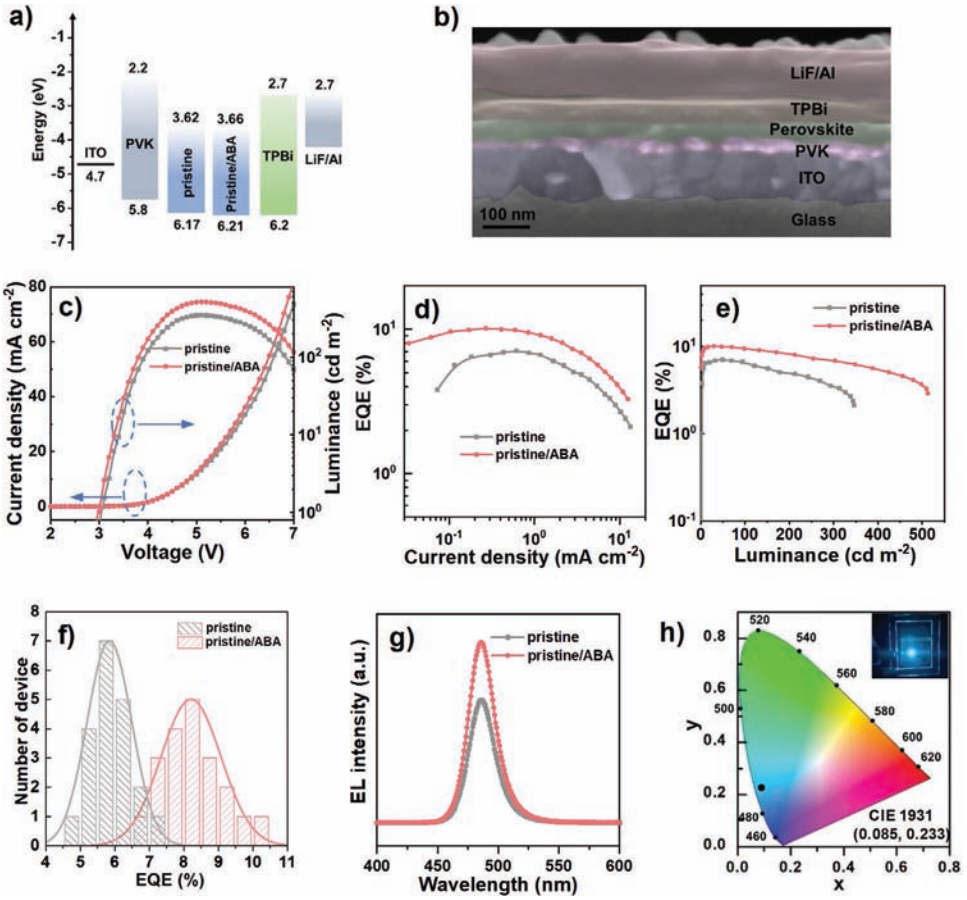

Figure 4. PeLED structure and performance: a) the energy diagram of each layer in PeLEDs, b) the cross-section scanning electron microscopy (SEM) image of PeLEDs, c) density–luminance–voltage (*J–L–V*), d) ef ciency–current density (*EQE–J*), and e) ef ciency–luminance (*EQE–L*) curves. f) Histograms of 20 devices for each pristine and pristine/ABA PeLEDs. The average EQE of pristine and pristine/ABA PeLEDs is 5.84% and 8.21% with a relative standard deviation of 11.1% and 10.6%, respectively. g) EL spectra of pristine and pristine/ABA PeLEDs, and h) the CIE coordinate of pristine/ABA PeLEDs with the emission image in the inset.

by ultraviolet photoelectron spectroscopy (UPS) (Figure S9, Supporting Information), and the band alignment of the functional layers in the whole device is summarized in **Figure 4**a. The thickness of PVK, perovskite emission layer, TPBi, and LiF/Al layers is around 26, 40, 45, and 100 nm, respectively, as determined from the cross-section scanning electron microscopy (SEM) image (Figure 4b). The SEM image also shows a more uniform film for pristine/ABA perovskite than pristine perovskite (Figure S10, Supporting Information), as further confirmed by the smaller surface roughness of 0.79 nm as compared to 1.05 nm for pristine perovskite. (Figure S11, Supporting Information). The smooth and dense perovskite film should benefit the suppression of current leakage,[47] while the current density of pristine/ABA PeLEDs is slightly larger than that of pristine PeLEDs, which can be attributed to the increased carrier mobility of pristine/ABA films (Figure S12, Supporting Information) deriving from the coupling between perovskite phases. The PeLED performances in Figure 4c show that the maximum brightness (L_{max}) of pristine PeLEDs is 345 cd m^{-2} achieved at a bias of 5.10 V, which is enhanced to 513 cd m^{-2} for pristine/ABA devices. Meanwhile, there is a dramatic increase of EQE from 7.07% (pristine) to 10.11% for pristine/ABA PeLEDs (Figure 4d), consistent with this trend, the maximum current efficiency (CE) enhances from 8.12 to 11.87 cd A^{-1} (Figure S13, Supporting Information). Besides, the pristine/ABA PeLEDs maintain a decent efficiency with an efficiency droop of 32% at around 300 cd m^{-2}, which is obviously superior to that of pristine PeLEDs with a severe efficiency droop of 54% (Figure 4e). The pristine/ABA PeLEDs also show decent reproducibility with average EQE of 8.21% obtained from 20 devices (Figure 4f). The EL peaks of pristine and pristine/ABA PeLEDs are centered at 486 nm (Figure 4g), which are consistent with their PL spectra, implying that the EL is merely generated from the perovskites. In addition, the pristine/ABA PeLEDs show a narrowband emission with the full width at half maximum (FWHM) of around 25 nm, which enables an excellent color purity with Commission Internationale de L'Eclairage (CIE) chromaticity coordinate at (0.085, 0.233) (Figure 4h). We also investigated the effect of different ABA concentrations on the PeLED performances (Figure S15, Supporting Information). It is found that the highest EQE is achieved for 5% ABA incorporated PeLEDs. The performance will decline with further increase of the concentration to 10%, which can be ascribed to the deterioration of perovskite crystallinity at high ABA

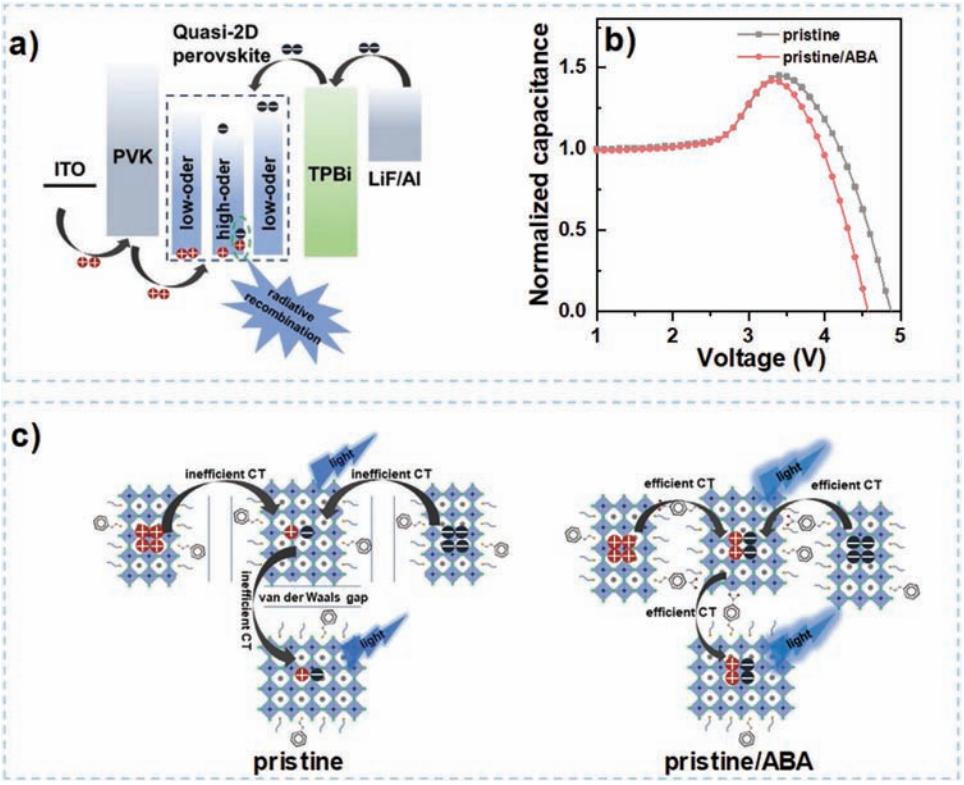

Figure 5. PeLED charge transfer characteristics: a) the working principle of quasi-2D PeLEDs, b) the PeLED capacitance–voltage (*C*–*V*) measurements, and c) illustration of charge transfer (CT) in pristine and pristine/ABA PeLEDs.

concentration (Figure S16, Supporting Information). Besides, the effect of PVK thickness on the device performance was also studied as shown in Figure S17 (Supporting Information), in which the PeLEDs based on 4 mg mL^{-1} PVK show the best performance, while the EQE decreases at higher concentrations due to the poor hole transport property for thicker PVK layers.

During the operation of quasi-2D PeLEDs, the injected charges (i.e., electrons and holes) accumulate and recombine at high-order perovskite due to the cascade energy structure of quasi-2D perovskites[63] (**Figure 5**a). Therefore, an efficient charge transfer between quasi-2D perovskite layers is important to obtain high PeLED performances. In order to study the charge transfer and recombination capacity of pristine and pristine/ABA PeLEDs, the capacitance–voltage (*C*–*V*) measurements were performed (Figure 5b). The capacitance enlarges when the bias voltage increases, indicating that the charges are injected into the PeLEDs. At higher voltage, the capacitance will sharply decline due to the largely reduced carriers caused by the radiative recombination of mass electrons and holes.[64] It is observed that the capacitance of pristine/ABA PeLEDs decreases faster than that of pristine PeLEDs at high voltages, indicating an efficient charge transfer for more radiative recombination of electrons and holes in pristine/ABA perovskite as illustrated in Figure 5c. To further verify the efficient charge transfer for high radiative recombination rate, we also carried out the electrical simulations of the PeLEDs (Figure S18, Supporting Information). The result shows that the peak radiative recombination rate for pristine/ABA PeLEDs increases near 40% to 1.71 10^{22} cm^3 s^{-1} from pristine PeLEDs (1.23 10^{22} cm^3 s^{-1}). Overall, we show that the efficient charge transfer in pristine/ABA perovskite promotes the larger radiative recombination of electrons and holes, which contributes to brighter pristine/ABA PeLEDs.

The excellent spectra stability for PeLEDs is important for their practical applications. However, it is a challenging issue to achieve spectrally stable blue PeLEDs, probably due to ion migration under high driving voltage and phase instability with Joule heating.[51,65] The EL spectra of pristine and pristine/ABA PeLEDs under different bias voltages from 4 to 8 V are recorded as shown in **Figure 6**a,b. It is observed that the EL intensity of pristine/ABA PeLEDs increases when the bias voltage increases from 4 to 5 V, and then declines at higher bias. Expectantly, the EL peak position (486 nm) and FWHM (25 nm) remain unchanged, indicating a good spectral stability under different bias voltages (Figure 6b). Similar to the situation of pristine/ABA PeLEDs, the spectra of pristine PeLEDs also remain stable in spite of the variation of EL intensity (Figure 6a). These results undoubtedly prove the excellent spectral stability for our mixed-ligand perovskite systems. Regarding the operational stability, we performed the lifetime tests of the devices under continuous constant current driving due to the generally current driving LEDs. We traced the efficiency of the PeLEDs under a constant current of 0.30 mA cm^{-2} which can generate the highest EQE of 8.65% for pristine/ABA PeLEDs. It is observed that the lifetime T_{50} (defined as the elapsed time of device decaying to 50% of its initial efficiency under continuous operation) for pristine/ABA PeLEDs is 81.3 min (Figure 6d), which is over 2.5-fold than that of the pristine PeLEDs (32.1 min) (Figure 6c). The longer

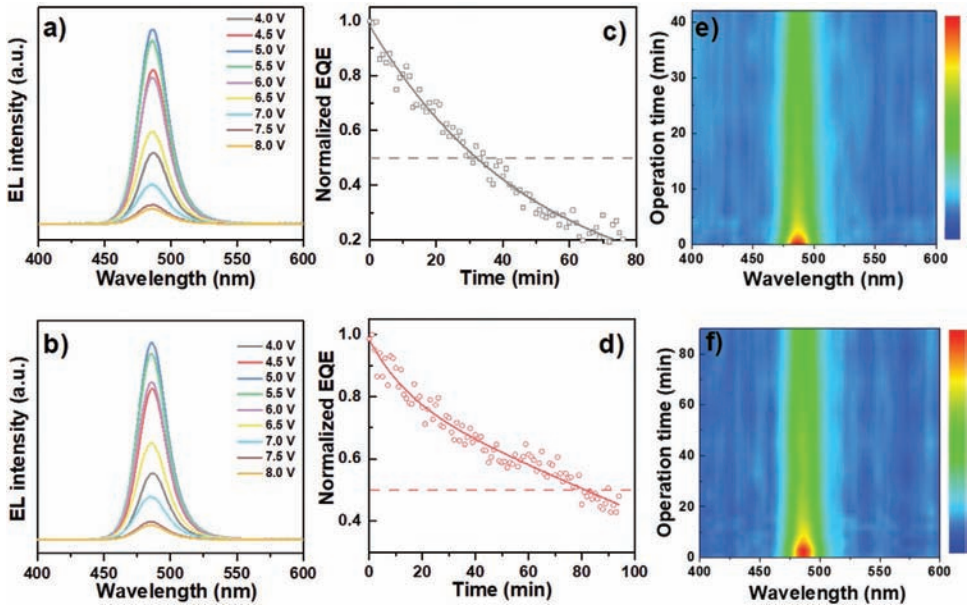

Figure 6. PeLED stability measurements: a,b) EL spectra at dif erent bias voltages, and c,d) the time-dependent stability lifetime measurements, and e,f) the traced EL spectra under constant current of 0.3 mA cm^{-2} during continuous operation of pristine and pristine/ABA blue PeLEDs corresponding to the initial EQE of 6.11% and 8.65%, respectively.

operational stability of the pristine/ABA PeLEDs was further verified at a high injection current (Figure S19, Supporting Information), which can be attributed to the less defects of the perovskite films and the built strong interaction between perovskite phases. Since the van der Waals gaps between the perovskite phases can destabilize the perovskite structure and thus the device,[52] our results of diminishing the weak van der Waals gap between perovskite phases through the bifunctional ABA can prolong the stability of PeLEDs. Meanwhile, the EL spectra of pristine/ABA PeLEDs under continuous operation remain unchanged as extending the operation time, revealing an excellent spectral stability during operation (Figure 6f). It shall be noted that the bias voltage increases along with the operation time as shown in Figure S20 (Supporting Information), showing the increased device resistance during operation. Consequently, our results show that the pristine/ABA PeLEDs show excellent spectral and operational stability, which is comparable with the reported stability of green and red analogs, signaling a great potential for blue PeLEDs toward practical applications.

In summary, we report to promote the coupling of quasi-2D perovskite layers with reduction of the weak van der Waals gap between perovskite layers by the bifunctional group of amino and carboxylic of ABA. By in-depth study of the optical and electrical properties of pristine/ABA perovskites, we demonstrate that the ABA incorporated perovskites benefit an efficient energy transfer between quasi-2D perovskite layers and thus enhance the radiative recombination rate. Simultaneously, the ABA can reduce traps states by suppression of metallic Pb. Combined the two advantages from the bifunctional ABA incorporation, a high-performance blue PeLEDs with external quantum efficiency of 10.11% (average EQE of 8.21%) is achieved, which is increased over 40% than that of pristine PeLEDs (7.07%, average EQE of 5.84%). Meanwhile, the pristine/ABA PeLEDs show a prolonged operational stability of T_{50} 81.3 min, which is over 2.5-fold than that of the pristine PeLEDs (32.1 min) and represents one of the most stable blue PeLEDs reported so far. Consequently, our work paves an effective way to realize high-performance and stable blue PeLEDs toward practical application.

Experimental Section

Materials: Propylamine hydrobromide (PABr, 99.999%), and phenethylammonium hydrobromide (PEABr, 99.999%) were purchased from Greatcell Solar; 4-(2-Aminoethyl)benzoic acid (ABA, 97%), Cesium trif uoroacetate ($Cs(CF_3COO^-)$, 99.999%), $PbBr_2$ (99.999%), and HBr (48% wt in H_2O) were bought from Sigma-Aldrich. Poly(9-vinylcarbazole) (PVK), Tris(1-phenyl-1H-benzimidazol-2-yl)benzene (TPBi, 99.5%) and LiF (99.99%) were purchased from Lumtec.

ABA_2PbBr_4 Synthesis: Generally, 5 mmol 4-(2-aminoethyl)benzoic acid was added into 10 mL deionized water, then 0.68 mL HBr aqueous solution was dropped to the solution. After stirring for 2 h at 0 C, the solution was rotary evaporated to obtain the precipitate, which was successively washed with ethanol and diethyl ether for several times, then dried at 60 C for 12 h to obtain ABABr powders. ABA_2PbBr_4 perovskite precursor was prepared by dissolving ABABr and $PbBr_2$ in DMSO at the molar ratio of 2:1 and stirring at 70 C for 12 h.

Perovskite Emission Layer Preparation: $CsPbBr_3$ powder was first synthesized according to the previous method.[15] The precursor of $PEA_xPA_{2-x}(CsPbBr_3)_{n-1}PbBr_4$ perovskite was prepared by dissolving 0.15 m $CsPbBr_3$ powder, 0.15 m PABr, and 0.015 m PEA_2PbBr_4 into DMSO. Then the pristine $PEA_xPA_{2-x}(CsPbBr_3)_{n-1}PbBr_4$ perovskite films were obtained by spin-coating the precursor at 3000 rpm for 60 s in which 300 L of toluene was quickly dripped on the substrate at 28 s after the spin-procedure starting, followed by annealing at 75 C for 10 min. For the pristine/ABA perovskites, the precursor were prepared by adding dif erent concentrations of ABA_2PbBr_4 into the $PEA_xPA_{2-x}(CsPbBr_3)_{n-1}PbBr_4$ solution (e.g., 5% ABA incorporated perovskite precursor was prepared by adding 3.75 10^{-3} m ABA_2PbBr_4 into pristine perovskite precursor).

Device Fabrication: The glass/ITO substrates were successively washed by deionized water, acetone, and isopropyl alcohol, and then further

cleaned with UV-Ozone cleaner for 20 min. The PVK HIL was prepared by spin-coating the PVK solution (4 mg mL^{-1} dissolved in chlorobenzene) on ITO substrates at 4000 rpm for 45 s, and then heated at 120 C for 15 min before use. The perovskite precursor solution was spin-coated on PVK substrates for preparation of the perovskite films. Then TPBi, LiF, and Al electrode were successively evaporated onto the perovskite films with the thickness of 45, 1, and 100 nm at deposition rates of 0.5, 0.04, and 1 Å s^{-1}, respectively. After completion of the device fabrication, the devices were sealed by an ultraviolet-curable resin before testing.

Characterization: UV–vis absorption spectra were performed with the spectrophotometer of PERSEE TU-1901. X-ray dif raction analysis was carried on X-ray dif ractometer (Bruker Advance D8 Ew Germany) with Cu Kα radiation. The morphology of perovskite films and the cross-sectional SEM characterization were performed on the scanning electron microscope (Zeiss 1550). The XPS measurements were carried out with Kratos Ultra Spectrometer equipped with monochromatized Al Kα X-ray photons discharge lamp. The UPS analysis was carried out using a KRATOS ULTRA AXIS DLD photoelectron spectroscopy system with an unfiltered He I (21.22 eV) gas-discharge lamp. AFM images were measured with use of the atomic force microscope of NanoScope III (Digital Instrument). The PLQY were recorded by the equipment of Hamamatsu Quantaurus-QY, model no. C11347. TA spectroscopy was conducted using an ExciPro XL Femtosecond Transient Absorption Pump-Probe Spectrometer (CDP systems). The perovskite films were pumped with a femtosecond 365 nm laser pulse generated from an optical parametric amplifier. The probe pulses ranging from 380 to 800 nm were derived from the fundamental 800 nm laser pulses with a small portion (5 J) of a 2 mm thick CaF_2 plate. The steady-state and time-resolved photoluminescence of perovskite were performed on PicoQaunt FluoTime 300 equipped with a picosecond pulse laser (360 nm, LDH-P-C-360) with a pulse width of 40 ps. The time-resolved photoluminescence was conducted by a time-corrected single photon counting (TCSPC, PicoHarp 300E) module equipped with a photomultiplier (PMA-C 192-M) detector. The capacitance–voltage (*C*–*V*) measurement was carried out with use of Keithley 4200A parameter analyzer at 1 kHz and 30 mV AC amplitude. The tDOS experiment was performed using Keithley 4200A parameter analyzer with the frequency range from 10^3 to 10^7 Hz and 25 mV AC amplitude. The *t*DOS (N_T) can be derived from the angular frequency dependent capacitance with the equation: $N_T = -\frac{V_{bi}}{qW}\frac{dC}{d\omega}\frac{\omega}{k_BT}$, where *C* is the capacitance, ω is the angular frequency, *q* is the elementary charge, k_B is the Boltzmann constant, *T* is the temperature, V_{bi} is the built-in potential, and *W* is the depletion width, respectively. The current density–voltage–luminance curves were obtained from Ocean Optics system equipped with a Keithley 2400 source meter, an integrating sphere (FOIS-1), and an QE Pro spectrometer. The integrating sphere was calibrated with a radiometric calibration light source (HL-3plus) before use. The active area for the devices is 4 mm^2. The EQEs of perovskite LEDs are obtained by measuring the light intensity in the forward direction by placing the devices on the top of the integrating sphere. The scanning rate is 0.5 V s^{-1} with a dwell time of 1.5 s. The device performances are crosschecked at University of Hong Kong (W. C. group) and Southern University of Science and Technology (K. W. group) to show the reliable result. The CIE coordinates of the devices were obtained from LED Color Calculator (OSRAM).

Supporting Information

Supporting Information is available from the Wiley Online Library or from the author.

Acknowledgements

This research was supported by Equipment fund, Platform Research Fund and feed fund (Grant Nos. 2019157209, 201511159225, and 201811159147), from the University Grant Council of the University of Hong Kong, the General Research Fund (Grant Nos. 17211220, 17204117, and 17200518) from Hong Kong Special Administrative Region, China, as well as 2019B121205001 from Department of Science and Technology of Guangdong Province, National Science Foundation (NSF) of China (No. 61875082), National Key Research and Development Program (No. 2017YFE0120400), and NSF of Guangdong Province (No. 2017B030306010). The authors acknowledge Xiangtian Xiao and Zhaojin Wang for their help in characterization.

Conf ict of Interest

The authors declare no conf ict of interest.

Keywords

blue perovskite LEDs, defect passivation, energy transfer

Received: August 17, 2020
Revised: October 20, 2020
Published online: November 20, 2020

[1] Z.-K. Tan, R. S. Moghaddam, M. L. Lai, P. Docampo, R. Higler, F. Deschler, M. Price, A. Sadhanala, L. M. Pazos, D. Credgington, F. Hanusch, T. Bein, H. J. Snaith, R. H. Friend, *Nat. Nanotechnol.* **2014**, 9, 687.
[2] M. Yuan, L. N. Quan, R. Comin, G. Walters, R. Sabatini, O. Voznyy, S. Hoogland, Y. Zhao, E. M. Beauregard, P. Kanjanaboos, Z. Lu, D. H. Kim, E. H. Sargent, *Nat. Nanotechnol.* **2016**, 11, 872.
[3] M. V. Kovalenko, L. Protesescu, M. I. Bodnarchuk, *Science* **2017**, *358*, 745.
[4] Q. A. Akkerman, G. Rainò, M. V. Kovalenko, L. Manna, *Nat. Mater.* **2018**, 17, 394.
[5] H. Cho, S.-H. Jeong, M.-H. Park, Y.-H. Kim, C. Wolf, C.-L. Lee, J. H. Heo, A. Sadhanala, N. Myoung, S. Yoo, S. H. Im, R. H. Friend, T.-W. Lee, *Science* **2015**, *350*, 1222.
[6] M. K. Gangishetty, S. Hou, Q. Quan, D. N. Congreve, *Adv. Mater.* **2018**, *30*, 1706226.
[7] S. A. Veldhuis, P. P. Boix, N. Yantara, M. Li, T. C. Sum, N. Mathews, S. G. Mhaisalkar, *Adv. Mater.* **2016**, 28, 6804.
[8] K. Lin, J. Xing, L. N. Quan, F. P. G. De Arquer, X. Gong, J. Lu, L. Xie, W. Zhao, D. Zhang, C. Yan, W. Li, X. Liu, Y. Lu, J. Kirman, E. H. Sargent, Q. Xiong, Z. Wei, *Nature* **2018**, 562, 245.
[9] Y. Cao, N. Wang, H. Tian, J. Guo, Y. Wei, H. Chen, Y. Miao, W. Zou, K. Pan, Y. He, H. Cao, Y. Ke, M. Xu, Y. Wang, M. Yang, K. Du, Z. Fu, D. Kong, D. Dai, Y. Jin, G. Li, H. Li, Q. Peng, J. Wang, W. Huang, *Nature* **2018**, 562, 249.
[10] B. Zhao, S. Bai, V. Kim, R. Lamboll, R. Shivanna, F. Auras, J. M. Richter, L. Yang, L. Dai, M. Alsari, X.-J. She, L. Liang, J. Zhang, S. Lilliu, P. Gao, H. J. Snaith, J. Wang, N. C. Greenham, R. H. Friend, D. Di, *Nat. Photonics* **2018**, 12, 783.
[11] F. Zhang, B. Cai, J. Song, B. Han, B. Zhang, H. Zeng, *Adv. Funct. Mater.* **2020**, *30*, 2001732.
[12] H. Wang, Y. Xu, J. Wu, L. Chen, Q. Yang, B. Zhang, Z. Xie, *J. Phys. Chem. Lett.* **2020**, 11, 1411.
[13] K.-H. Wang, Y. Peng, J. Ge, S. Jiang, B.-S. Zhu, J. Yao, Y.-C. Yin, J.-N. Yang, Q. Zhang, H.-B. Yao, *ACS Photonics* **2019**, 6, 667.
[14] S. T. Ochsenbein, F. Krieg, Y. Shynkarenko, G. Rainò, M. V. Kovalenko, *ACS Appl. Mater. Interfaces* **2019**, 11, 21655.
[15] Z. Ren, X. Xiao, R. Ma, H. Lin, K. Wang, X. W. Sun, W. C. H. Choy, *Adv. Funct. Mater.* **2019**, 29, 1905339.

[16] Q. Wang, J. Ren, X.-F. Peng, X.-X. Ji, X.-H. Yang, *ACS Appl. Mater. Interfaces* **2017**, 9, 29901.
[17] Z. Chen, C. Zhang, X.-F. Jiang, M. Liu, R. Xia, T. Shi, D. Chen, Q. Xue, Y.-J. Zhao, S. Su, H.-L. Yip, Y. Cao, *Adv. Mater.* **2017**, 29, 1603157.
[18] D. N. Congreve, M. C. Weidman, M. Seitz, W. Paritmongkol, N. S. Dahod, W. A. Tisdale, *ACS Photonics* **2017**, 4, 476.
[19] Y. Dong, Y.-K. Wang, F. Yuan, A. Johnston, Y. Liu, D. Ma, M.-J. Choi, B. Chen, M. Chekini, S.-W. Baek, L. K. Sagar, J. Fan, Y. Hou, M. Wu, S. Lee, B. Sun, S. Hoogland, R. Quintero-Bermudez, H. Ebe, P. Todorovic, F. Dinic, P. Li, H. T. Kung, M. I. Saidaminov, E. Kumacheva, E. Spiecker, L.-S. Liao, O. Voznyy, Z.-H. Lu, E. H. Sargent, *Nat. Nanotechnol.* **2020**, 15, 668.
[20] F. Yang, H. Chen, R. Zhang, X. Liu, W. Zhang, J. Zhang, F. Gao, L. Wang, *Adv. Funct. Mater.* **2020**, 30, 1908760.
[21] B.-B. Zhang, S. Yuan, J.-P. Ma, Y. Zhou, J. Hou, X. Chen, W. Zheng, H. Shen, X.-C. Wang, B. Sun, O. M. Bakr, L.-S. Liao, H.-T. Sun, *J. Am. Chem. Soc.* **2019**, 141, 15423.
[22] S. Hou, M. K. Gangishetty, Q. Quan, D. N. Congreve, *Joule* **2018**, 2, 2421.
[23] J. Pan, L. N. Quan, Y. Zhao, W. Peng, B. Murali, S. P. Sarmah, M. Yuan, L. Sinatra, N. M. Alyami, J. Liu, E. Yassitepe, Z. Yang, O. Voznyy, R. Comin, M. N. Hedhili, O. F. Mohammed, Z. H. Lu, D. H. Kim, E. H. Sargent, O. M. Bakr, *Adv. Mater.* **2016**, 28, 8718.
[24] J. Song, J. Li, X. Li, L. Xu, Y. Dong, H. Zeng, *Adv. Mater.* **2015**, 27, 7162.
[25] G. Li, F. W. R. Rivarola, N. J. L. K. Davis, S. Bai, T. C. Jellicoe, F. De La Peña, S. Hou, C. Ducati, F. Gao, R. H. Friend, N. C. Greenham, Z.-K. Tan, *Adv. Mater.* **2016**, 28, 3528.
[26] R. L. Z. Hoye, M.-L. Lai, M. Anaya, Y. Tong, K. Gałkowski, T. Doherty, W. Li, T. N. Huq, S. Mackowski, L. Polavarapu, J. Feldmann, J. L. Macmanus-Driscoll, R. H. Friend, A. S. Urban, S. D. Stranks, *ACS Energy Lett.* **2019**, 4, 1181.
[27] W. Deng, X. Jin, Y. Lv, X. Zhang, X. Zhang, J. Jie, *Adv. Funct. Mater.* **2019**, 29, 1903861.
[28] Y. Wu, C. Wei, X. Li, Y. Li, S. Qiu, W. Shen, B. Cai, Z. Sun, D. Yang, Z. Deng, H. Zeng, *ACS Energy Lett.* **2018**, *3*, 2030.
[29] D. Yang, Y. Zou, P. Li, Q. Liu, L. Wu, H. Hu, Y. Xu, B. Sun, Q. Zhang, S.-T. Lee, *Nano Energy* **2018**, 47, 235.
[30] S. Peng, S. Wang, D. Zhao, X. Li, C. Liang, J. Xia, T. Zhang, G. Xing, Z. Tang, *Small Methods* **2019**, *3*, 1900196.
[31] S. Kumar, J. Jagielski, S. Yakunin, P. Rice, Y.-C. Chiu, M. Wang, G. Nedelcu, Y. Kim, S. Lin, E. J. G. Santos, M. V. Kovalenko, C.-J. Shih, *ACS Nano* **2016**, 10, 9720.
[32] D. Liang, Y. Peng, Y. Fu, M. J. Shearer, J. Zhang, J. Zhai, Y. Zhang, R. J. Hamers, T. L. Andrew, S. Jin, *ACS Nano* **2016**, 10, 6897.
[33] Y. Jin, Z.-K. Wang, S. Yuan, Q. Wang, C. Qin, K.-L. Wang, C. Dong, M. Li, Y. Liu, L.-S. Liao, *Adv. Funct. Mater.* **2020**, 30, 1908339.
[34] T. L. Leung, H. W. Tam, F. Liu, J. Lin, A. M. C. Ng, W. K. Chan, W. Chen, Z. He, I. Lončarić, L. Grisanti, C. Ma, K. S. Wong, Y. S. Lau, F. Zhu, Ž Skoko, J. Popović, A. B. Djurišić, *Adv. Opt. Mater.* **2020**, 8, 1901679.
[35] D. Ma, P. Todorović, S. Meshkat, M. I. Saidaminov, Y.-K. Wang, B. Chen, P. Li, B. Schef el, R. Quintero-Bermudez, J. Z. Fan, Y. Dong, B. Sun, C. Xu, C. Zhou, Y. Hou, X. Li, Y. Kang, O. Voznyy, Z.-H. Lu, D. Ban, E. H. Sargent, *J. Am. Chem. Soc.* **2020**, 142, 5126.
[36] N. Yantara, N. F. Jamaludin, B. Febriansyah, D. Giovanni, A. Bruno, C. Soci, T. C. Sum, S. Mhaisalkar, N. Mathews, *ACS Energy Lett.* **2020**, 5, 1593.
[37] P. Vashishtha, M. Ng, S. B. Shivarudraiah, J. E. Halpert, *Chem. Mater.* **2019**, *31*, 83.
[38] A. Sadhanala, S. Ahmad, B. Zhao, N. Giesbrecht, P. M. Pearce, F. Deschler, R. L. Z. Hoye, K. C. Gödel, T. Bein, P. Docampo, S. E. Dutton, M. F. L. De Volder, R. H. Friend, *Nano Lett.* **2015**, 15, 6095.
[39] J. Xing, Y. Zhao, M. Askerka, L. N. Quan, X. Gong, W. Zhao, J. Zhao, H. Tan, G. Long, L. Gao, Z. Yang, O. Voznyy, J. Tang, Z.-H. Lu, Q. Xiong, E. H. Sargent, *Nat. Commun.* **2018**, 9, 3541.
[40] X. Yang, X. Zhang, J. Deng, Z. Chu, Q. Jiang, J. Meng, P. Wang, L. Zhang, Z. Yin, J. You, *Nat. Commun.* **2018**, 9, 570.
[41] N. K. Kumawat, X.-K. Liu, D. Kabra, F. Gao, *Nanoscale* **2019**, 11, 2109.
[42] Z. Li, Z. Chen, Y. Yang, Q. Xue, H.-L. Yip, Y. Cao, *Nat. Commun.* **2019**, 10, 1027.
[43] Y. Liu, J. Cui, K. Du, H. Tian, Z. He, Q. Zhou, Z. Yang, Y. Deng, D. Chen, X. Zuo, Y. Ren, L. Wang, H. Zhu, B. Zhao, D. Di, J. Wang, R. H. Friend, Y. Jin, *Nat. Photonics* **2019**, *13*, 760.
[44] Z. Ren, L. Li, J. Yu, R. Ma, X. Xiao, R. Chen, K. Wang, X. W. Sun, W.-J. Yin, W. C. H. Choy, *ACS Energy Lett.* **2020**, 5, 2569.
[45] F. Wang, Z. Wang, W. Sun, Z. Wang, Y. Bai, T. Hayat, A. Alsaedi, Z. A. Tan, *Small* **2020**, 16, 2002940.
[46] S. Yuan, Z.-K. Wang, L.-X. Xiao, C.-F. Zhang, S.-Y. Yang, B.-B. Chen, H.-T. Ge, Q.-S. Tian, Y. Jin, L.-S. Liao, *Adv. Mater.* **2019**, *31*, 1904319.
[47] Y. Jiang, C. Qin, M. Cui, T. He, K. Liu, Y. Huang, M. Luo, L. Zhang, H. Xu, S. Li, J. Wei, Z. Liu, H. Wang, G.-H. Kim, M. Yuan, J. Chen, *Nat. Commun.* **2019**, 10, 1868.
[48] F. Yuan, C. Ran, L. Zhang, H. Dong, B. Jiao, X. Hou, J. Li, Z. Wu, *ACS Energy Lett.* **2020**, 5, 1062.
[49] Q. Wang, X. Wang, Z. Yang, N. Zhou, Y. Deng, J. Zhao, X. Xiao, P. Rudd, A. Moran, Y. Yan, J. Huang, *Nat. Commun.* **2019**, 10, 5633.
[50] P. Pang, G. Jin, C. Liang, B. Wang, W. Xiang, D. Zhang, J. Xu, W. Hong, Z. Xiao, L. Wang, G. Xing, J. Chen, D. Ma, *ACS Nano* **2020**, 14, 11420.
[51] Y. Shang, Y. Liao, Q. Wei, Z. Wang, B. Xiang, Y. Ke, W. Liu, Z. Ning, *Sci. Adv.* **2019**, 5, eaaw8072.
[52] S. Ahmad, P. Fu, S. Yu, Q. Yang, X. Liu, X. Wang, X. Wang, X. Guo, C. Li, *Joule* **2019**, *3*, 794.
[53] S.-C. Yun, S. Ma, H.-C. Kwon, K. Kim, G. Jang, H. Yang, J. Moon, *Nano Energy* **2019**, 59, 481.
[54] S. Yang, J. Dai, Z. Yu, Y. Shao, Y. Zhou, X. Xiao, X. C. Zeng, J. Huang, *J. Am. Chem. Soc.* **2019**, 141, 5781.
[55] J. Byun, H. Cho, C. Wolf, M. Jang, A. Sadhanala, R. H. Friend, H. Yang, T.-W. Lee, *Adv. Mater.* **2016**, 28, 7515.
[56] L. Xie, J. Chen, P. Vashishtha, X. Zhao, G. S. Shin, S. G. Mhaisalkar, N.-G. Park, *ACS Energy Lett.* **2019**, 4, 2192.
[57] D. Bi, C. Yi, J. Luo, J.-D. Décoppet, F. Zhang, S. M. Zakeeruddin, X. Li, A. Hagfeldt, M. Grätzel, *Nat. Energy* **2016**, 1, 16142.
[58] T. Wu, Y. Wang, X. Li, Y. Wu, X. Meng, D. Cui, X. Yang, L. Han, *Adv. Energy Mater.* **2019**, 9, 1803766.
[59] R. Quintero-Bermudez, A. Gold-Parker, A. H. Proppe, R. Munir, Z. Yang, S. O. Kelley, A. Amassian, M. F. Toney, E. H. Sargent, *Nat. Mater.* **2018**, 17, 900.
[60] J. Liu, J. Leng, K. Wu, J. Zhang, S. Jin, *J. Am. Chem. Soc.* **2017**, 139, 1432.
[61] D. Shi, V. Adinolfi, R. Comin, M. Yuan, E. Alarousu, A. Buin, Y. Chen, S. Hoogland, A. Rothenberger, K. Katsiev, Y. Losovyj, X. Zhang, P. A. Dowben, O. F. Mohammed, E. H. Sargent, O. M. Bakr, *Science* **2015**, *347*, 519.
[62] Q. Dong, Y. Fang, Y. Shao, P. Mulligan, J. Qiu, L. Cao, J. Huang, *Science* **2015**, *347*, 6225.
[63] N. Wang, L. Cheng, R. Ge, S. Zhang, Y. Miao, W. Zou, C. Yi, Y. Sun, Y. Cao, R. Yang, Y. Wei, Q. Guo, Y. Ke, M. Yu, Y. Jin, Y. Liu, Q. Ding, D. Di, L. Yang, G. Xing, H. Tian, C. Jin, F. Gao, R. H. Friend, J. Wang, W. Huang, *Nat. Photonics* **2016**, 10, 699.
[64] X. Qu, N. Zhang, R. Cai, B. Kang, S. Chen, B. Xu, K. Wang, X. W. Sun, *Appl. Phys. Lett.* **2019**, 114, 071101.
[65] H. Cho, Y.-H. Kim, C. Wolf, H.-D. Lee, T.-W. Lee, *Adv. Mater.* **2018**, *30*, 1704587.